Research Repository UCD

Title	Investigation of AFM-based machining of ferroelectric thin films at the nanoscale
Authors(s)	Zhang, Fengyuan, Edwards, David, Deng, Xiong, Kilpatrick, J. I., Rodriguez, Brian J., et al.
Publication date	2020-01-17
Publication information	Zhang, Fengyuan, David Edwards, Xiong Deng, J. I. Kilpatrick, Brian J. Rodriguez, and et al. "Investigation of AFM-Based Machining of Ferroelectric Thin Films at the Nanoscale." American Institute of Physics, January 17, 2020. https://doi.org/10.1063/1.5133018.
Publisher	American Institute of Physics
Item record/more information	http://hdl.handle.net/10197/11992
Publisher's statement	This article may be downloaded for personal use only. Any other use requires prior permission of the author and AIP Publishing. This article appeared in Zhang, F., Edwards, D., Deng, X., Wang, Y., Kilpatrick, J.I., Bassiri-Gharb, n. Kumar, A. Chen, D., Gao, X. and Rodriguez, B.J. Investigation of AFM-based machining of ferroelectric thin films at the nanoscale. Journal of Applied Physics 127 (3), Article Number: 034103, and may be found at https://doi.org/10.1063/1.5133018.
Publisher's version (DOI)	10.1063/1.5133018

Downloaded 2026-05-01 23:37:22

The UCD community has made this article openly available. Please share how this access benefits you. Your story matters! (@ucd_oa)

© Some rights reserved. For more information

Journal of Applied Physics ARTICLE scitation.org/journal/jap

Investigation of AFM-based machining of ferroelectric thin films at the nanoscale

Cite as: J. Appl. Phys. **127**, 034103 (2020); doi: 10.1063/1.5133018
Submitted: 22 October 2019 · Accepted: 17 December 2019 ·
Published Online: 17 January 2020

Fengyuan Zhang,[1,2,a)] David Edwards,[1,2,a)] Xiong Deng,[3] Yadong Wang,[3] Jason I. Kilpatrick,[1,2] Nazanin Bassiri-Gharb,[4,5] Amit Kumar,[6] Deyang Chen,[3] Xingsen Gao,[3] and Brian J. Rodriguez[1,2,b)]

AFFILIATIONS

[1]School of Physics, University College Dublin, Belfield, Dublin D04 V1W8, Ireland
[2]Conway Institute of Biomolecular and Biomedical Research, University College Dublin, Belfield, Dublin D04 V1W8, Ireland
[3]Institute for Advanced Materials, South China Academy of Advanced Optoelectronics, Guangzhou 510006, People's Republic of China
[4]School of Materials Science and Engineering, Georgia Institute of Technology, Atlanta, Georgia 30332-0405, USA
[5]George W. Woodruff School of Mechanical Engineering, Georgia Institute of Technology, Atlanta, Georgia 30332-0405, USA
[6]Centre for Nanostructured Media, School of Mathematics and Physics, Queen's University Belfast, Belfast BT7 1NN, United Kingdom

[a)]**Contributions:** Fengyuan Zhang and David Edwards contributed equally to this work.
[b)]**E-mail:** brian.rodriguez@ucd.ie

ABSTRACT

Atomic force microscopy (AFM) has been utilized for nanomechanical machining of various materials including polymers, metals, and semiconductors. Despite being important candidate materials for a wide range of applications including data storage and actuators, ferroelectric materials have rarely been machined via AFM. AFM-based machining of ferroelectric nanostructures offers advantages over established techniques, such as bottom-up approaches and focused ion beam milling, in select cases where low damage and low-cost modification of already-fabricated thin films are required. Through a systematic investigation of a broad range of AFM parameters, we demonstrate that AFM-based machining provides a low-cost option to rapidly modify local regions of the film, as well as fabricate a range of different nanostructures, including a nanocapacitor array with individually addressable ferroelectric elements.

Published under license by AIP Publishing. https://doi.org/10.1063/1.5133018

I. INTRODUCTION

Physical modification of functional materials at the nanoscale is essential for numerous nanotechnology-based applications, as well as fundamental investigations into their functional behavior.[1] One of the approaches to achieve this end is atomic force microscopy (AFM)-based machining, where a force is applied via a sufficiently stiff AFM probe to mechanically remove materials locally from the sample.[2–4] Also referred to as mechanical scanning probe lithography or nanomechanical machining, this technique has been utilized in a number of recent studies to, e.g., fabricate complex arrays of 3D nanodots on polycarbonate samples[5] and nanochannels of varying depth in silicon,[6] reproduce photographs on a polished aluminum disk[7] and form single photon emitters via nanoindentations on a polymer film.[8] The analysis of AFM-based machining behavior has been utilized to characterize the hardness of materials in nanoscale sclerometry measurements,[9] and AFM-based machining has also been used to precisely remove materials from regions of the sample surface in tomography investigations.[10–13] Given the simplicity of this approach, one would expect that it could be adapted to ferroic materials, which find extensive applications in data storage, and, in particular, to ferroelectric oxides where there is strong interest in both the fabrication of nanostructures[14] and volumetric investigations.[15–17] Despite this promising capability, few AFM-based machining studies have been applied to ferroelectrics[18–20] (i.e., materials possessing a spontaneous polarization that is reversible under an applied electric field). One notable exception is the recent work by Steffes *et al.*,[18] where volumetric imaging of ferroelectric domains in a $BiFeO_3$ thin film was

Published under license by AIP Publishing.

achieved through sequential nanometric removal of layers of the film with a large (~11.4 μN) loading force, while monitoring the domain structure via piezoresponse force microscopy (PFM).

The electric-field switchable polarization of ferroelectrics along with large piezoelectric response, nanoscale conductive anomalies, and above bandgap photovoltaic behavior enables a range of potential applications relevant to data storage, nanoelectronics, and sensors.[21,22] With the continuing miniaturization of electronic devices, numerous studies have focused on the fabrication of ferroelectric nanostructures so as to minimize the size of the switchable ferroelectric elements.[23] The effects of mechanical boundary conditions such as epitaxial strain, substrate clamping, and localized stress have been shown to have a pronounced effect on the properties of a number of ferroelectric materials.[24–27] As such, studies have also involved the fabrication of ferroelectric nanostructures as a means to alter the mechanical boundary conditions imposed on the ferroelectric material and provide further physical insight into different ferroelectric phenomena mediated through the release of mechanical constraints.[26,28,29] Such nanostructures have conventionally been fabricated through a range of bottom-up (mask-assisted pulsed laser deposition,[30] block copolymer self-assembly[31]) and top-down [focused ion beam (FIB),[32] electron beam writing,[33] and AFM tip-assisted crystallization[34]] techniques. In ferroelectric samples, tomography investigations have typically been achieved by carefully polishing relaxor ferroelectric ceramic samples,[35] repeated surface chemical etching of bulk Pb(Zr,Ti)O_3,[36] or via nondestructive confocal Raman microscopy of both periodically poled as well as more complex dendritic electrically-induced domains in $LiNbO_3$.[37,38] In this context, AFM-based machining provides an alternative low-cost option to both fabricate nanostructures as well as undertake tomographic functional investigations, while avoiding problems related to ion-injection from FIB,[39] mask limitations (where the nanostructure is limited by the shape and dimensions of the mask) with mask-assisted bottom-up approaches[14] and low resolution (~1 μm) of confocal Raman microscopy.[18] The AFM setup also enables data to be collected *in situ* during the machining process, thereby providing insight into the mechanical as well as functional properties, such as the conductivity of the material.[18] In order to exploit these advantages, the technique must be able to reliably machine a broad range of depths into the ferroelectric sample and also be able to fabricate reproducible nanostructures with small (<100 nm) lateral dimensions for high-density applications. The sensitivity and precision of AFM enables a range of parameters such as loading force, tip velocity, scan angle, etc. to be varied; all of which can be used to control the machining process, as has been observed on a range of different materials.[40–42] However, the effect of these parameters on a ferroelectric thin film is largely unknown. In particular, the effect of loading forces exceeding 20 μN, where larger depths (10s of nm) of materials can be removed in a single pass of the AFM tip, has not been investigated. In examining the effect of these parameters, the capability and limitations of the technique to fabricate ferroelectric nanostructures need to be explored.

In this work, we systematically investigate the effect of AFM parameters on the machining behavior of an epitaxially-strained thin film of $BiFeO_3$, a lead-free ferroelectric where the epitaxial constraint gives rise to coexistence of different phases. Such films are prime candidates for magnetoelectric, piezoelectric, and nanoelectronic devices.[43–45] Here, the conditions required to thin local regions of such a mixed phase $BiFeO_3$ film to a range of depths are theoretically predicted and experimentally demonstrated. These conditions could be utilized for the fabrication of complex 3D nanostructures, measurements of certain properties as a function of thickness, or in some cases alterations of ferroelectric properties due to local changes in the film thickness.[18,46] A framework is established to determine the optimum conditions required to fabricate nanostructures with the smallest lateral dimensions possible in the film. Finally, the possibility of fabricating a range of different nanostructures is explored.

II. MATERIALS AND METHODS

In this work, ~50 nm thick epitaxial $BiFeO_3/Ca_{0.67}Ce_{0.33}MnO_3/LaAlO_3$ and $BiFeO_3/LaSrMnO_3/LaAlO_3$ films were used. Both films were fabricated by pulsed laser deposition with a KrF excimer laser ($\lambda = 248$ nm). The laser fluence and repetition rate were fixed at 0.63 J/cm^2 and 8 Hz, respectively. The target to substrate distance was set at 5.5 cm, while the films were deposited in an ambient oxygen pressure of 15 Pa and a deposition temperature of 680–700 °C. Cr-Au electrodes ~ 70 μm in diameter comprising 5 nm of Cr and 2 nm of Au were evaporated onto the $BiFeO_3/Ca_{0.67}Ce_{0.33}MnO_3$ film through a shadow mask using an electron beam evaporator (DE400, DE Technology, USA) at a rate of 0.4 Å/s in vacuum. Electrodes comprising 5 nm of Cr and 0.5 nm of Au were evaporated onto the $BiFeO_3/LaSrMnO_3$ film. Data are shown for the $BiFeO_3/Ca_{0.67}Ce_{0.33}MnO_3$ film unless otherwise specified.

Diamond AFM probes (NM-RC and NM-TC, Adama Innovations Ltd., Ireland) with a spring constant, *k*, of 130.57 N/m and 117.07 N/m, respectively (as calibrated via the Sader method),[47] were used in a contact mode for all machining operations. It should be noted that the spring constant calibration can have an uncertainty of up to ±10%.[48] The deflection sensitivity of both cantilevers was determined by carrying out a 10 × 10 array of force distance curves, post-machining, on a thick diamond film, providing values of 46.6 ± 0.1 nm/V for the NM-TC tip and 44.1 ± 0.1 nm/V for the NM-RC tip. To extract mechanical properties and fabricate nanostructures, the NM-RC probes were used, which have a nominal tip radius of 10 ± 5 nm. NM-TC probes were used for the thinning experiments and have a larger nominal radius of 25 ± 10 nm. Both probe types have a ~90° opening angle. The residual pileup of materials due to machining operations was subsequently removed by imaging of the region with a small, nondestructive loading force (~1 μN) using the same diamond probe (demonstrated in Fig. S1 of the supplementary material). Before and after each machining experiment, the profiles of the diamond probes were evaluated by blind tip reconstruction, after scanning a tip characterization grating (TGT101, MikroMasch, Germany) in amplitude modulation mode, as shown in Fig. S2 of the supplementary material.[49,50] Although the diamond probes are also capable of imaging the resulting machined features (see Fig. S1 of the supplementary material), sharp Si probes (PPP-NCHR, Nanosensors, Switzerland) were used in amplitude modulation mode to obtain all of the topography images shown in this work to minimize any artefacts due to machined residue on the tip or the oblique opening angle of the diamond probes. Conductive $PtIr_5$ coated Si probes (PPP-EFM, Nanosensors, Switzerland) were used to acquire contact-mode piezoresponse and conductivity images. All experiments were carried out using a commercial AFM (Cypher, Asylum Research, USA). It should

Published under license by AIP Publishing.

be noted that the inclination angle between the cantilever and sample is ∼11°, while the sample typically had a tilt of ∼1°–2° with respect to the cantilever, as determined from unflattened images. For each experiment, the cantilever was loaded into the cantilever holder such that it aligned with the 0° axis, as determined optically, with an estimated uncertainty of ±1°. Vertical PFM (VPFM) images and local hysteresis loops were obtained using the built-in Dual AC Resonance Tracking (DART) mode, with a 1 V_{AC} imaging bias, centered around a contact resonance frequency of ∼330 kHz.[51]

III. RESULTS AND DISCUSSION

A. AFM-based machining for material thinning

A key aspect of AFM-based machining involves material removal to thin local regions of the sample. As mentioned previously, this would have direct implications toward the fabrication of 3D nanostructures, tomography related applications, and/or probing novel ferroelectric phenomena. For optimal thinning to be realized, the ability to reliably predict depths and achieve a desired smoothness of the machined surface is required. Here, 500 nm × 500 nm regions are machined by scanning the NM-TC tip from top to bottom with a large loading force over a number of closely spaced (10, 30, and 60 nm) adjacent lines. The machining was carried out via single pass lines (i.e., lines were drawn manually in the lithography mode so no retrace was carried out) to compare the results to the nanochannel depth prediction model described by Geng *et al.*[52] The removal depth and resulting roughness (root mean squared, *rms*) were examined as a function of varying applied loading force, separation between adjacent machined lines, and tip velocity.

Figure 1(a) shows the AFM topography image of a region of the film after the application of varying loading forces using three different separation distances between adjacent lines. This was carried out at a constant velocity of 0.25 μm/s, which was selected based on preliminary testing. The mixed phase $BiFeO_3$ film consists of a rhombohedral-like R phase, which comprises the banded needlelike structures, within a tetragonal-like T phase matrix. Due to a combination of the tip size and a possible softening of material adjacent to the machined regions (which is then removed during the machining of

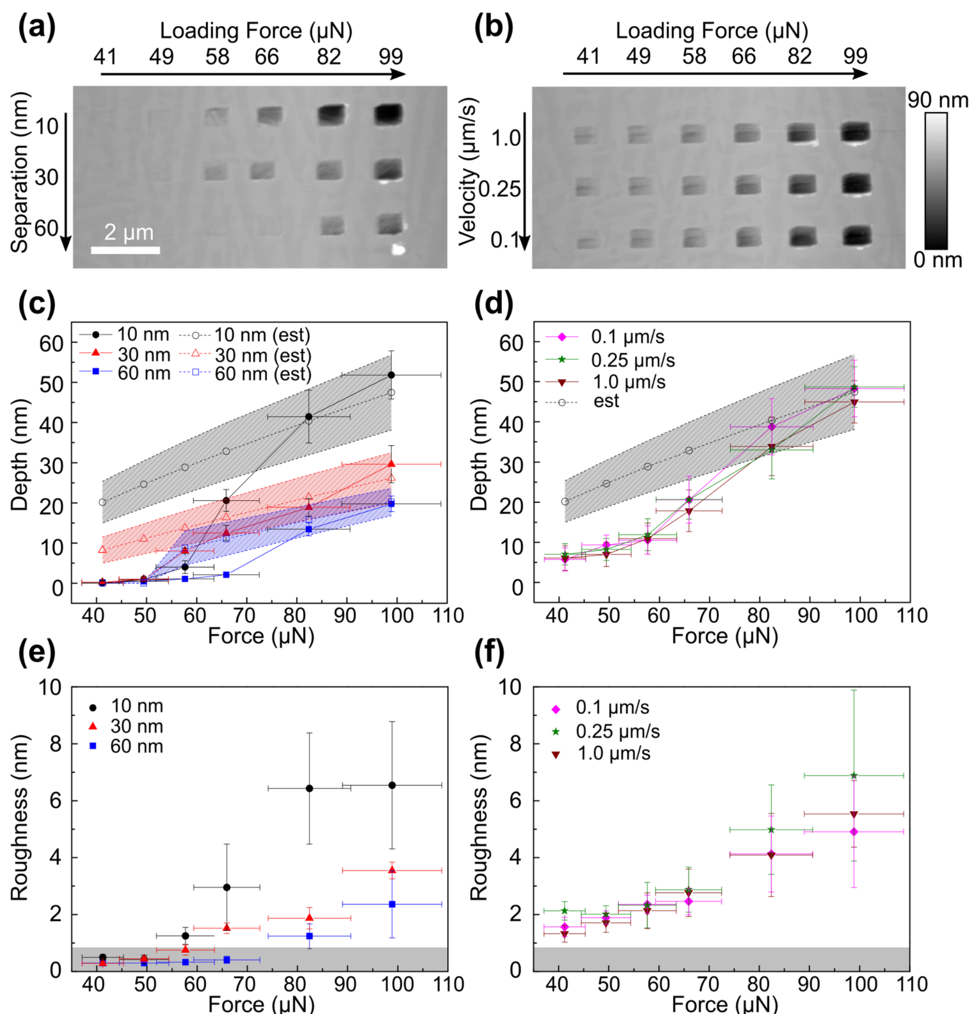

FIG. 1. Effect of different AFM parameters on the thinning of local regions of a mixed phase $BiFeO_3$ film. (a) Topography after applying a matrix of loading forces and separations between adjacent scan lines at a constant velocity of 0.25 μm/s. (b) Topography after applying a matrix of loading forces and tip velocities at a constant line-separation of 10 nm. Variation in machined (c) depth and (e) roughness (rms) from (a). The dashed lines with hollow symbols labeled "est" describe the corresponding depths estimated by the nanochannel depth prediction model.[52] Variation in machined (d) depth and (f) roughness (rms) from (b). Values in (e) and (f) where machining has occurred can be seen to have a larger roughness than 0.8 ± 0.2 nm (rms) of the as-grown film, which is represented by the gray shaded region. The applied force values have an uncertainty of ±10%.[48]

Published under license by AIP Publishing.

subsequent lines), the resulting machined boxes have rectangular dimensions of approximately 1000×500 nm. At a glance, it can be seen that the largest line-separations and lowest loading forces result in no material removal. The machining depth increases with loading force and decreases with line-separation. The average depth and roughness of each machined box (analyzed over a constant area per box) is shown quantitatively in Figs. 1(c) and 1(e), respectively. The depth was obtained by first aligning (via MATLAB) the topography images before and after machining, such that the difference in height on the unmachined regions of the before and after images was minimized. The average height of an array of 25×25 pixels within the machined squares was then subtracted from the average height of an array of pixels over the same region before it was machined so as to account for the initial variations in height due to the mixed phase topography. The scans before and after machining were taken with the same pixel density (512×512 pixels over $100\,\mu m^2$), such that the sample area over which the change in depth is measured is the same. The depth and standard deviation values are plotted in Figs. 1(c) and 1(d). For the largest line-separation of 60 nm, which is slightly larger than the measured NM-TC tip radius of ∼40 nm (see Fig. S2 of the supplementary material), machining does not occur until $82\,\mu$N is applied. In contrast, for the lowest line-separation of 10 nm, machining occurs for loading forces $\geq 49\,\mu$N. The machined depth at $99\,\mu$N load also increases dramatically from 17 ± 2 nm for 60 nm line-separation, to 45 ± 6 nm for 10 nm line-separation, highlighting the strong effect of varying line-separation with the increased overlap between adjacent machined lines at low separations effectively enabling repeated machining over the same regions and an increased depth.[6,49] The shallowest machined depth of 0.9 ± 0.3 nm was obtained with a $49\,\mu$N load at a 10 nm line-separation. This is similar to the gradual (<1 nm) removal of materials observed in a number of previous works.[10,13,18] In the aforementioned studies, such gradual removal was initiated, in some cases, after repeated scanning with a relatively smaller (∼$11\,\mu$N) loading force. Hence, it is feasible that repeated scanning with the parameters where no machining was observed may lead to comparable behavior, i.e., removal of materials in a manner similar to that associated with the ploughing regime, where plastic deformation begins to occur.[41,53] As expected, the larger forces used here enabled a more rapid removal of materials.

Additionally, a 3×6 grid of 500×500 nm regions was machined at a constant line-separation of 10 nm, while varying the tip velocity and applied loading force. The topography of these machined regions is shown in Fig. 1(b), while the measured depth and roughness are shown in Figs. 1(d) and 1(f), respectively. Little variation in the depth or roughness is observed with different tip velocities, except at larger loading forces (≥$58\,\mu$N), where a slight increase in the depth is observed at the two slower tip velocities within the errors. At the largest force and slowest tip velocity, the depth obtained was 56 ± 3 nm, exceeding the film thickness and resulting in the partial removal of the bottom electrode. When machining to depths approaching the film thickness, it is difficult to determine whether or not the bottom electrode has been partially machined; however, assuming the bottom electrode has a similar or lower yield stress compared to the $BiFeO_3$ film (as both materials are perovskite films), it is likely that some of the bottom electrode was removed as well. Some deviation in depth between the squares machined by identical parameters in the machining experiment is evident, as shown in Figs. 1(c) and 1(d). More specifically, the physical removal of material begins at a lower loading force in the experiment using a varying velocity, in comparison to the experiment using a constant velocity. This deviation highlights additional uncertainty at low loading forces that could occur due to variations in the tip contact area across the surface, mechanically-induced phase transformations,[45] machined pileup at the tip apex, and a reduction in the tip-sample friction, which is known to occur at low machining depths.[41] Meanwhile, the machined depths at larger loading forces are more consistent between experiments. Such behavior is analogous to FIB milling, where additional considerations are required in some cases when milling to nanoscale depths, as opposed to microscale depths.[54,55]

In analyzing the roughness more closely—as a function of line-separation and loading force in Fig. 1(e), and tip velocity and force in Fig. 1(f)—the clearest trend is the increase in roughness with depth. For instance, at the lowest machined depths (0.9 ± 0.3 nm), the measured roughness (0.8 nm) is similar to the average roughness measured across various 500×500 nm regions of the as-grown sample (0.8 ± 0.2 nm), as indicated by the baseline in Figs. 1(e) and 1(f). While at increased depths, the roughness reaches much higher values of 3–8 nm. The dispersion in roughness values despite identical machining parameters being used in some cases [e.g., $66\,\mu$N at $0.25\,\mu$m/s and 10 nm line-separation in Figs. 1(e) and 1(f)] further highlights the aforementioned deviation in machining behavior, which could also be related to factors such as redeposition of machined residues. Although the roughness values at varying separations appear similar, the increased depth at 10 nm line spacing alludes to that particular separation enabling the deepest and smoothest machining. Additionally, it may be possible to machine large depths, via application of larger loading forces, and reduce the roughness via subsequent scans with lower (∼ 40–60 μN) forces in a "cut and polish" type of approach. Meanwhile, no clear variation in roughness is observed with varying tip velocities as has been observed in AFM-based machining studies on other materials.[56]

Experimental data were compared to predictions made from the model used by Geng *et al.*[52] This model was chosen as it accounts for line-separation and does not require precise values of Young's modulus, which is known to exhibit substantial variations in mixed phase $BiFeO_3$, both spatially across the film (between the R and T phases) and with a range of different values quoted in the literature.[57–59] The model approximates the machining process as a hard abrasive particle sliding over a softer sample. The loading force (F_N) is given as the product of the yield stress, σ_y, multiplied by the horizontally projected area of interface A_T,

$$F_N = \sigma_y A_T, \tag{1}$$

where A_T is dependent on the line-separation Δ, as well as the effective tip radius R' at the machined depth h. As shown in Fig. S2(f) of the supplementary material, the tip used here can be approximated by a truncated cone with a tip half-angle (α_{tha}) of $54 \pm 1°$ with a flat circular apex with a radius of 39.5 ± 0.5 nm. Hence, A_T can be approximated as follows:[52]

$$\begin{aligned} A_T = &\frac{1}{3}(2R' - \Delta)\sqrt{(2R' - \Delta)\Delta} + \frac{1}{2}\arccos\frac{R' - \Delta}{R'}R'^2 \\ &- \frac{1}{2}(R' - \Delta)\sqrt{R'^2 - (R' - \Delta)^2}, \end{aligned} \tag{2}$$

Published under license by AIP Publishing.

where R' is described in terms of h, the tip radius R_0 and α_{tha},

$$R' = (h - R_0(1 - \sin\alpha_{tha}))\tan\alpha_{tha} + R_0\cos\alpha_{tha}. \quad (3)$$

Using the value for σ_y of 71.1 ± 15.9 GPa, as estimated from AFM nanoindentation experiments (Fig. S3 of the supplementary material), the predicted machined depth h can be determined using the above equation. These are shown as dashed lines in Figs. 1(c) and 1(d). The large uncertainties propagate from the uncertainty in σ_y. The estimated depths tend to compare well at larger loading forces but deviate at lower loading forces. This may be due to the model not accounting for factors such as elastic recovery, friction, surface roughness, structural phase transitions, and the influence of the machined pileup material. Such observations are similar to those previously obtained on metals,[52] where larger machined depths (>50 nm) were predicted more accurately than smaller ones.

The ability to control the machined depth in thin films enables the study of the variation in properties as a function of depth, as well as fabricating 3D nanostructures. As a basic example of the former, a conductive AFM (cAFM) scan (Fig. S4 of the supplementary material) demonstrates that current increases for machined depths of ≥ 50 nm, indicating that the tip has machined through the insulating ferroelectric film to the conductive bottom electrode below. Such observations can provide an indication of the film thickness, with an average estimated thickness of 48 ± 1 nm.

B. AFM-based machining for nanostructure fabrication

In exploring the potential of AFM-based machining for nanostructure fabrication, a crucial aspect involves the determination of the sharpest possible feature (i.e., maximum depth and minimum width) that can be reliably fabricated with the AFM tip. Nominally, this would depend on parameters related to the profile of the tip (such as the half-angle and tip radius) as well as the film thickness. For instance, the $BiFeO_3$ film is ∼50 nm thick, while the reconstructed profile of the NM-RC tip (used for the remaining experiments in this work) can be modeled by a rounded cone with a radius of 2.5 nm and a half-angle of 43°. From this, the diameter of the tip at 50 nm from the apex is ∼105 nm in diameter, and so could ideally enable features to be machined through the thickness of the film that are slightly greater than ∼105 nm in width, or features that have a depth of 5 nm and width of ∼25 nm, with the tip being effectively utilized as a nanoscale diamond scribe. To determine if these depth *vs.* width relationships hold true, we investigated the effect of different AFM parameters on the machined depth and width of single lines.

The effect of machining angle, α_m, (i.e., the direction of the tip relative to the sample) on machined depth and width was examined by machining a series of circles encompassing the effect of all possible angles. To exclude external effects such as the crystallization direction of the film and the tip-sample azimuthal angle, the sample was physically rotated counterclockwise to 4 different angles (0°, 32°, 62°, and 90°). Figure 2(a) shows the topography

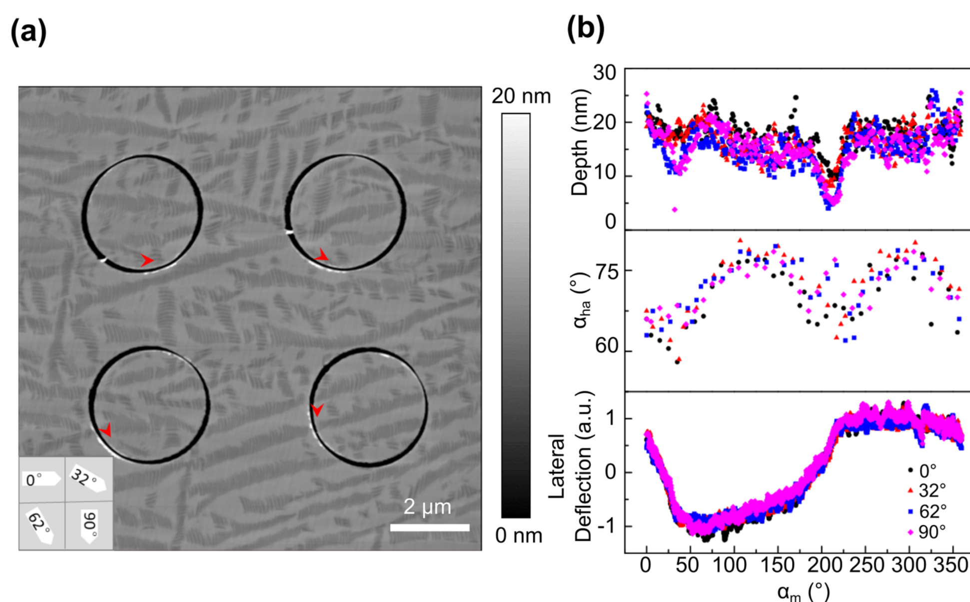

FIG. 2. The effect of machining angle. (a) Topography of a 12 × 12 μm region of the $BiFeO_3$ film after machining four circles that are 2.5 μm in diameter using a loading force of 70 μN at 0.5 μm/s. The sample was rotated to 0° (top left), 32° (top right), 62° (bottom left), and 90° (bottom right) for the four circles, so as to isolate machining angle-related effects. The inset image in (a) shows the cantilever (white arrow) angle with respect to the sample (gray background) which corresponds to each circle. The red arrows show the machining direction and position where the machining angle is 0°. α_m is defined as the angle between the long axis of the cantilever and the tip motion direction as schematized in Fig. S5 of the supplementary material. (b) The machined depth, machined α_{ha} (half-angle of the machined line), and the lateral deflection of tip vs α_m for different sample rotation angles.

Published under license by AIP Publishing.

after machining the circles at these four rotated angles at a constant force of 70 μN with a 0.5 μm/s tip velocity. These force and tip velocity values were chosen based on preliminary measurements resulting in significant machined depths without exceeding the thickness of the thin film. The red arrow in each circle represents the tip location and machining direction at 0° (i.e., when the machining angle is parallel to the long axis of the cantilever). The value of the machined depth and half-angle of the machined line, α_{ha} (indicative of width and sharpness), at each α_m was then determined by cross-section analysis across the machined lines (schematized in Fig. S5 of the supplementary material). Each of the four machined circles shows similar variations in machined depth and α_{ha} with α_m, as shown in Fig. 2(b), thereby excluding nonmachining angle-related effects.

Another advantage of using AFM in these studies is that data can be acquired *in situ* during machining. The lateral deflection signal, proportional to the force across the short axis of the cantilever, is shown in Fig. 2(b) (reset to 0 prior to each machining). The machined depth is minimized when α_m corresponds to ∼30° and ∼210°, at similar values of α_m where the lateral deflection shows local maxima or minima. Although α_{ha} also shows local minima at these α_m, as the machined depth is at a minimum, these angles are a suboptimal choice for achieving the sharpest possible machined features. Meanwhile, α_{ha} shows a strong variation with different machining angles; for instance, α_{ha} is smaller for a range of α_m values at ∼0°–50° and ∼180°–220°, when approximately parallel to the cantilever long axis, compared to at $\alpha_m \sim 90°$ and ∼270°, which is perpendicular to the long axis of the cantilever. This variation can be explained by the fact that the calculated spring constant parallel to the cantilever long axis is almost twice that of the spring constant parallel to the short axis (see the supplementary material).[60] This observation is also evident in lateral deflections shown in Fig. 2(b), as the signal measured when machining roughly parallel to the cantilever long axis is closer to zero compared to other machining angles. An increased lateral deflection and torsion of the cantilever, in turn results in a larger α_{ha} and a wider machined trench due to the geometry of the tip-sample contact. For example, if the tip rotates ∼10° around the short axis when $\alpha_m \sim 90°$, we can assume that the tip would only rotate ∼5° around the long axis when $\alpha_m \sim 0°$, as it is known (from above) that the cantilever is almost twice as stiff along the latter direction. From studying the reconstructed tip, this additional ∼5° tilt would result in a ∼15% increase in a contact area at a 15 nm depth. The influence of the cantilever lateral deflection or torsion on the resulting depth and width has also been suggested in previous AFM-based machining studies on other materials, where the torsion is caused by a combination of friction and the resistance of the material to deformation during the machining process.[43] Such an effect could be obviated by utilizing a stiffer cantilever. Although the lateral deflection reaches zero at ∼10°–20°, this could be due to the increased machined depth which occurs at 0°, in turn resulting in increased torsion. Further study of the machined depth and α_{ha} of straight lines at varying machining angles can be found in Fig. S5 of the supplementary material. We conclude that a machining angle of 0° can be used to machine the sharpest possible features.

In order to fabricate nanoscale structures using an AFM tip, it is also essential to study the effect of different loading forces and tip velocities on the depth and width [defined as schematized in Fig. S5(b) of the supplementary material] of a single machined line. Figure 3(a) shows a series of straight lines machined with different tip velocities from 0.125 to 2 μm/s from left to right and with different loading forces from 17 to 86 μN from top to bottom. All lines were machined at $\alpha_m = 0°$, as it was previously established to give the sharpest machining. At each loading force, the tip velocity was observed to have little effect on the depth of the machined lines, which is similar to what has been observed on other materials.[40] Machining began for tip velocities <2 μm/s at 17 μN, and the machined depth increased significantly with the increasing force (∼0.085 nm/μN). The machined depths were also predicted using the nanomechanical model used by Geng *et al.*[52] for machining single lines, where

$$A_T = \frac{1}{2}\pi(R_0 \cos\alpha_{tha} + (h - R_0 + R_0 \sin\alpha_{tha}) \tan\alpha_{tha})^2. \quad (4)$$

The NM-RC tip was modeled as a rounded cone with an α_{tha} of 47° and an R_0 of 2.5 nm, as shown in Fig. S2 of the supplementary material. Repeatability is also evident here, e.g., at a loading force of ∼69 μN and a tip velocity of 0.5 μm/s, the machined depth (∼24 nm) agrees with the corresponding machined depth in Fig. 2. α_{ha} was observed to decrease with increasing loading force. This demonstrates that α_{ha} is larger for the shallowest machined lines, likely due to the larger half-angle of the tip itself close to the apex. However, based on the dispersion in the data and the size of the error bars, it is unclear if α_{ha} stabilizes or continues to decrease at higher loading forces. The width of the machined lines appears to increase linearly with loading force up until ∼43 μN, after which the rate of increase slows. The width also appears to be affected by tip velocity. For instance, at larger loading forces, faster tip velocities result in features that are up to ∼40 nm wider than at slower velocities. It should be noted that when carrying out the experiment, the lines were machined in the order from the slowest to the fastest velocities, and so these results may be influenced by an accumulation of machined materials on the tip. Moreover, when carrying out part of the experiment in a reverse order, as shown in Fig. S6 of the supplementary material, the variation appears more random, highlighting that velocity likely has a more subtle effect on the machining behavior. Meanwhile, the relatively large width and α_{ha} of the machined lines compared to the reconstructed profile of the tip could be attributed to the lateral tilt of the tip with the global 11 ± 2° inclination angle between the cantilever and sample, along with additional tilt during machining caused by lateral torsion or buckling of the cantilever. For example, if we account for this global inclination angle along with an additional, say ∼10° tilt during machining, the contact area estimated from the reconstructed tip at a machined depth of ∼15 nm increases by ∼45%, compared to a tip without any tilt. An additional factor contributing to the increased machined width could be the effect of mechanically induced phase transformations.

With the effects of different AFM parameters on the depth and width of machined features in this ferroelectric film determined, we proceed to fabricate nanostructures with the smallest lateral features enabled by this method. Here, simple square nanoislands were fabricated by machining two parallel lines at $\alpha_m = 0°$ separated by a defined distance that defines the lateral dimensions of the island. Subsequently, the sample was rotated by 90° and two

Published under license by AIP Publishing.

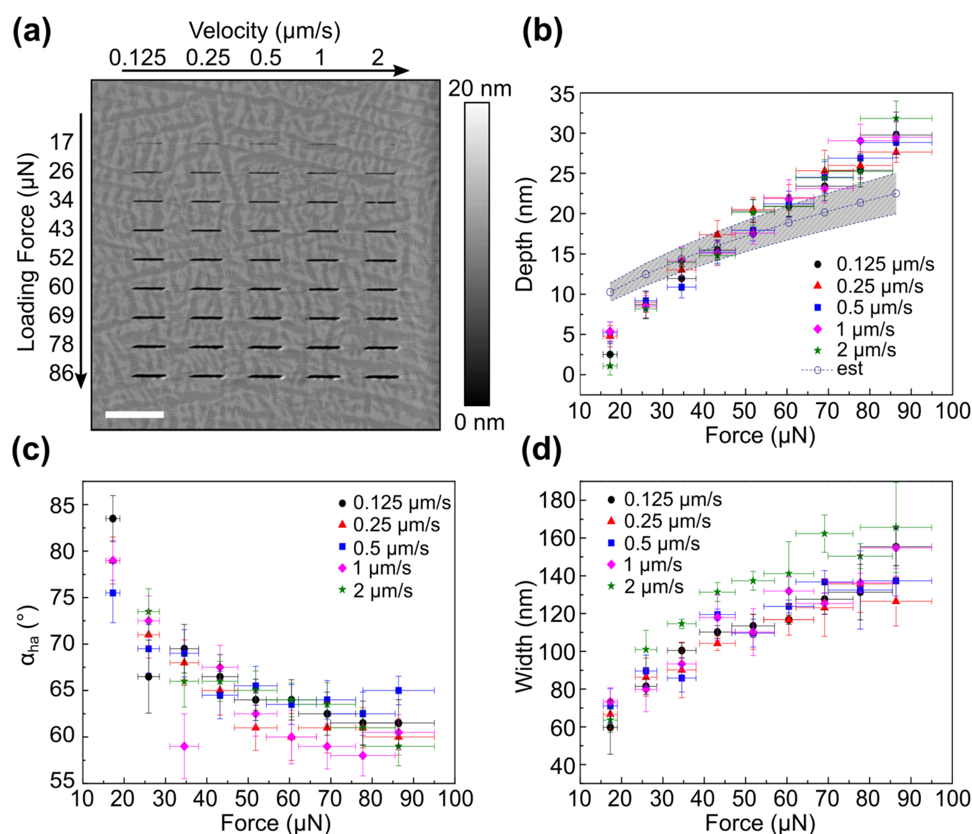

FIG. 3. The effect of varying tip velocity and loading force at a constant machining angle. (a) The topography of a 12 × 12 μm region of the $BiFeO_3$ film after machining a series of lines that are 1 μm in length with varying tip velocity and loading force. (b) Machined depth (with the theoretical estimates denoted by "est"), (c) half-angle and (d) width as analyzed from (a) as a function of loading force for different tip velocities. The scale bar is 2 μm.

more parallel lines, separated by the same defined distance were machined at $\alpha_m = 0°$ to create a single nanoisland. From Fig. 3, it was observed that a 17 μN loading force at 0.125 μm/s gave rise to a machined depth just below 5 nm and a width of ∼70 nm. Using the above parameters, a 90 × 90 nm nanoisland was machined, as shown in Fig. 4(a). The lines were machined longer than 90 nm, so as to accommodate for any microscope drift and guarantee overlap of the orthogonal lines. Line profiles corresponding to the vertical (red) and horizontal (blue) lines in the topography image are shown in Figs. 4(a)(ii) and 4(a)(iii), respectively. The blue horizontal line profiles across the first pair of lines machined show a depth of ∼5 nm, as expected. However, for the second pair of lines machined (red vertical lines), the machined depth increased to ∼10 nm despite the observation from Fig. 2 that rotating the sample had little effect on the machined depth. This increase in the machined depth with the same loading force could be caused by softening of the surrounding region after the first pair of lines were machined, as has been observed in other materials.[61] It could also be due to a jolting effect of the tip as it crosses orthogonally over the previously machined line; this effect is evident when monitoring the lateral deflection of the cantilever (Fig. S7 of the supplementary material), where a decrease in the lateral deflection is observed after crossing over the first previously machined line, which coincides with a subsequent increase in the machined depth. As evidenced by the line profiles, the top surface of the fabricated island is at the same height as the surrounding surface height, with the black lines highlighting the lateral dimensions of the island.

To increase the machined depth, a 52 μN loading force at 0.125 μm/s was chosen with an expected depth of ∼20 nm and a width of ∼100 nm (see Fig. 3). Using these parameters, a second nanoisland with 120 nm line-separation was fabricated [Fig. S8(a) of the supplementary material]. Similar to the smaller nanoisland, the line profiles again show that the first pair of lines machined (blue) have a depth of ∼15 nm, while the second pair of lines machined (red) are >25 nm deep. In this case, the width of the machined line does not increase as rapidly between depths of 15 and 25 nm, cf. 5 and 10 nm; this is likely similar to the effect discussed in Fig. 3, where α_{ha} was found to be larger for shallower machined lines.

The ferroelectric properties of these nanoislands were then examined. Figures 4(b)(i) and 4(a)(ii) show the DART VPFM amplitude and phase hysteresis loops acquired on the 90 nm island [see Fig. S8(b) of the supplementary material for the 120 nm nanoisland]. In both cases, full phase reversal is achieved, which is accompanied by a minimum in amplitude, as typically observed for ferroelectrics.[62] Compared to loops acquired on the as-grown film (Fig. S7 of the supplementary material), a slight increase in the coercive field at a negative bias from the tip (opposite to the initial polarization direction of the film) is observed. Similar increases in coercive fields have been observed on nanoislands machined by

Published under license by AIP Publishing.

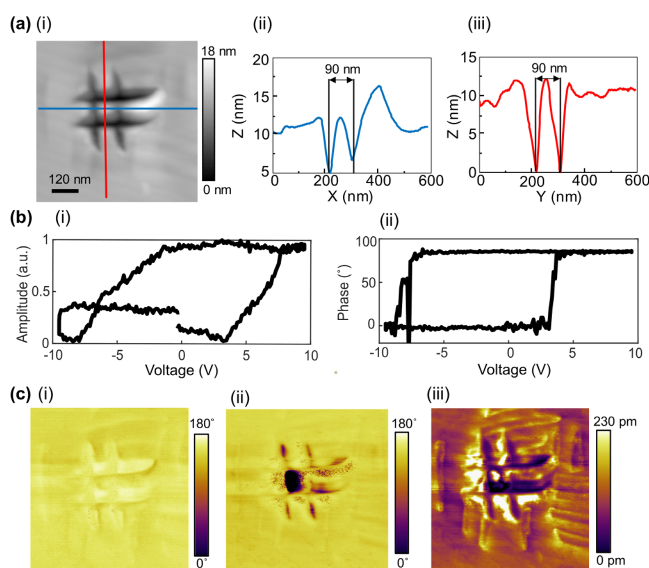

FIG. 4. Characterization of a 90 nm nanoisland. (a) (i) Topography and line profiles corresponding to the (ii) blue and (iii) red lines. (b) (i) VPFM amplitude and (ii) phase loop on the island. (c) VPFM phase image (i) before and (ii) after the acquisition of the hysteresis loop, showing the reversal of the measured phase from pointing down to up. (iii) VPFM amplitude after the loop acquisition showing a minimum in amplitude around the switched domain corresponding to the induced domain wall.

other methods on ferroelectric thin films and have been attributed to defects at the sidewalls of the islands causing increased pinning.[63] In order to further demonstrate the ferroelectricity of the nanoislands, DART VPFM images before and after loop acquisition are shown from the 90 and 120 nm nanoislands in Fig. 4(c) and Fig. S8(c) of the supplementary material, respectively. In both cases, the initial VPFM phase images [Fig. 4(c)(i)] show a uniform polarization pointing down toward the substrate. As the hysteresis loops were completed following the application of negative bias values, the resulting VPFM phase shows a reversal of polarization orientation pointing up toward the surface. The switched points were found to be stable over time and are accompanied by a minimum in the VPFM amplitude [Fig. 4(c)(iii)] at the domain walls. It should be noted that as the machined depth is less than the thickness of the film, switching may not be totally confined to the island as it is still connected to the surrounding film in the region adjacent to the bottom electrode. Nevertheless, the machined trench does appear to limit the propagation of domains from the island to the surrounding film (with one small needle domain propagating to the left of the switched location in the 120 nm island), as evidenced by the shape of the switched domain, which more strongly resembles the shape of the island itself. Another point of interest is that an increase in VPFM amplitude is observed around the periphery of the machined sections. Although possibly caused by topographic cross talk, such enhancement has also been observed in PFM studies of other ferroelectric samples that have been subjected to plastic indentation and has been attributed to the effect of residual tensile strain or increased dislocation activity around the indents.[64–66]

The dimensions of the nanoislands fabricated in this study highlight the limitations of AFM-based machining in fabricating ultrahigh-density nanostructures. For instance, the minimum lateral dimensions of 90 and 120 nm at depths of 5 and 20 nm are larger than the diameter of the reconstructed tip shown in Fig. S2 of the supplementary material of ∼25 and ∼65 nm at those depths. This difference is likely due to the previously mentioned factors, which result in a widening of the machined lines, including the lateral tilt of the tip during machining. However, despite AFM-based machining comparing unfavorably with bottom-up techniques, which have previously achieved sub-10 nm islands on ultrathin (<2 nm) films,[31] further improvements could easily be made using stiffer cantilevers, with a higher-aspect ratio tip on thinner films. Machining on a thinner film would reduce pileup and more easily enable machining through the thickness of films, in turn resulting in nanostructures that are isolated from the rest of the film. Indeed, a region of the film could potentially be thinned via machining before nanostructure fabrication. A higher-aspect ratio tip would reduce the limitation imposed by the shape of the tip, albeit such a change could come at the cost of lowering the stiffness. While a stiffer cantilever would feasibly result in reduced lateral torsion and deflection, which in turn may enable the widths of the machined features to be closer to the dimensions of the tip itself. This may also reduce the effect of α_m on the machining behavior, in turn enabling high-density nanostructures to be fabricated without the need to physically rotate the sample and restricted only by the tip velocities used here (up to 2 μm/s). Although different tips would give rise to different machining behavior, the ascribed approach provides a useful tool to characterize machining behavior and optimize the fabrication of nanostructures. Such a process could be further streamlined via machine-learning approaches.[67–70]

Furthermore, AFM-based machining can be readily used to fabricate a range of nanostructures and arrays. For example, more complex patterns can be fabricated, as demonstrated in Fig. 5(a) where a harp shape (the University College Dublin logo) has been machined by the tip on the $BiFeO_3/Ca_{0.67}Ce_{0.33}MnO_3$ film. A nanoarray consisting of islands 100×100 nm in size, fabricated on the $BiFeO_3$/LaSrMnO$_3$ film, is also shown in Fig. 5(b). The array was achieved through the same methods as described for Fig. 4, except with longer parallel lines, machined periodically over a larger area. Such arrays could feasibly be fabricated over the entire range of the AFM scanner (e.g., 30–100 μm, depending on the microscope used) and scaled-up even further through parallel processing, e.g., millipedelike schemes with arrays of stiff cantilevers.[71]

In addition to machining the bare surface of a ferroelectric film, AFM-based machining can also be carried out on deposited top-electrodes in order to fabricate a range of electrode structures. Here, a 5 nm film of Cr, followed by 2 nm of Au was evaporated onto a region of a mixed phase $BiFeO_3$ film. Cr was chosen as an electrode due to its low value of ductility and high brittleness,[72] enabling pileup from machining to be easily cleared, while having a top layer of Au is a commonly used technique to improve the electrical contact between the tip and the film via the electrode. Machining on thicker Au films was also attempted, however, the high ductility of Au led to persistent difficulties in removing

Published under license by AIP Publishing.

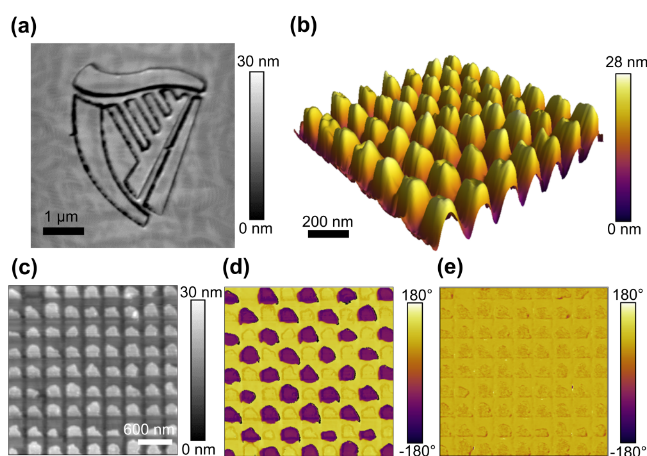

FIG. 5. Examples of nanostructures fabricated by AFM-based machining. Topography of (a) the University College Dublin harp logo machined on the $BiFeO_3/Ca_{0.67}Ce_{0.33}MnO_3$ film and (b) a 100 nm nanoisland array machined on the $BiFeO_3/LaSrMnO_3$ film. (c) Topography of a machined nanocapacitor array and the corresponding (d) VPFM phase after selectively switching elements with −10 V from the tip into a checkerboard pattern. (e) VPFM phase after applying +10 V to reverse the elements back to their initial state.

the pileup from machining. The electrode was chosen to be thin (total thickness 7 nm) so as to enable smaller electrode structures to be easily machined.

Prior to fabricating a nanoarray on the $BiFeO_3$-Cr-Au film, a similar procedure to that shown in Fig. 3 for the bare surface was carried out, as shown in Fig. S9 of the supplementary material. The topography of the fabricated nanocapacitor array is shown in Fig. 5(c). In this case, only the top electrodes are isolated while the bottom $Ca_{0.67}Ce_{0.33}MnO_3$ electrode is shared. We describe the resulting nanoarray as a nanocapacitor array, consistent with the terminology used to describe similar structures.[73,74] It can be seen that the top electrodes on some of the islands have delaminated, possibly due to poor adhesion. However, most of the nanocapacitor array remained intact. As demonstrated in Figs. 5(d) and 5(e), the elements are individually addressable and can be reversibly switched. Through an application of a negative bias (exceeding the coercive voltage) from the tip to selective elements in a checkerboard pattern, the polarization switches from pointing down, to pointing up, as indicated by the purple color in the VPFM phase image in Fig. 5(d). With the subsequent application of an above-coercive positive bias from the tip, these elements can then be reversed back to their initial state, as shown in Fig. 5(e).

IV. CONCLUSIONS

The capabilities and limitations of AFM-based machining of ferroelectric thin films have been systematically explored on epitaxially strained $BiFeO_3$. Machining using a broad range of loading forces, separation between adjacent lines, and tip velocities was found to locally thin regions of the film in a single pass to a range of depths by as little as subnanometers and as much as through the thickness of the film, into the underlying bottom electrode. Hence, the technique can be used to remove entire layers of materials and determine film thickness (in conjunction with cAFM), as well as remove multiple layers of different materials. The results were found to compare favorably to a nanochannel depth prediction model at larger loading forces, with larger deviations at lower forces. A process was also established to obtain nanostructures with the smallest possible lateral dimensions in the film. This involved analyzing the effect of different scanning angles, where it was found that scanning parallel to the cantilever long axis gave rise to the sharpest (i.e., deepest and narrowest) features. Examining the effect of different loading velocities and forces revealed that tip velocities had a minimal effect, while having a clean tip apex resulted in sharper features at each force and depth. From this, we were able to fabricate individually addressable ferroelectric nanostructures that were at least 5 nm and 20 nm deep, with respective widths of 90 nm and 120 nm. While the lateral dimensions of the islands were larger than the minimum size achievable based on the profile of the tip (∼25 and ∼65 nm at those depths), further improvements could be achieved with a stiffer, higher-aspect ratio tip. The possibility of fabricating a broad range of nanostructures was also demonstrated and machining could also be achieved on films with Cr-Au electrodes, enabling a proof-of-concept demonstration of a ferroelectric nanocapacitor array.

SUPPLEMENTARY MATERIAL

See the supplementary material for Figs. S1–S9 along with the relevant text.

ACKNOWLEDGMENTS

This publication has emanated from research supported in part by the China Scholarship Council and a research grant from Science Foundation Ireland (SFI) under the US-Ireland R&D Partnership Programme Grant No. SFI/14/US/I3113. This work was also supported by a research grant from SFI and the Sustainable Energy Authority of Ireland (SEAI) under the SFI Career Development Award Grant No. SFI/17/CDA/4637. N.B.-G. gratefully acknowledges support from the U.S. National Science Foundation (NSF) through Grant Nos. CMMI-1537262 and DMR-1255379. A.K. gratefully acknowledges support from Department of Education and Learning NI through grant USI-082 and Engineering and Physical Sciences Research Council via grant EP/S037179/1. D.C. acknowledges the National Natural Science Foundation of China (NNSFC) (Nos. U1832104 and 11704130). We acknowledge the helpful discussions with Professor Y. Yan. J.I.K. is partially funded by Adama Innovations Ltd., manufacturer of the diamond probes used in this study.

REFERENCES

[1]A. Biswas, I. S. Bayer, A. S. Biris, T. Wang, E. Dervishi, and F. Faupel, Adv. Colloid Interface Sci. **170**, 2 (2012).
[2]A. A. Tseng, A. Notargiacomo, and T. P. Chen, J. Vac. Sci. Technol. B **23**, 877 (2005).
[3]R. Magno and B. R. Bennett, Appl. Phys. Lett. **70**, 1855 (1997).
[4]Y. Yan, Y. Geng, and Z. Hu, Int. J. Mach. Tool Manuf. **99**, 1 (2015).
[5]Y. Yan, Y. Sun, J. Li, Z. Hu, and X. Zhao, Nanoscale Res. Lett. **9**, 372 (2014).

Published under license by AIP Publishing.

[6]U. Celano, F.-C. Hsia, D. Vanhaeren, K. Paredis, T. E. M. Nordling, J. G. Buijnsters, T. Hantschel, and W. Vandervorst, Sci. Rep. **8**, 2994 (2018).
[7]Y. Yan, Z. Hu, X. Zhao, T. Sun, S. Dong, and X. Li, Small **6**, 724 (2010).
[8]M. R. Rosenberger, C. K. Dass, H.-J. Chuang, S. V. Sivaram, K. M. McCreary, J. R. Hendrickson, and B. T. Jonker, ACS Nano **13**, 904 (2019).
[9]V. Blank, M. Popov, N. Lvova, K. Gogolinsky, and V. Reshetov, J. Mater. Res. **12**, 3109 (1997).
[10]U. Celano, L. Goux, A. Belmonte, K. Opsomer, A. Franquet, A. Schulze, C. Detavernier, O. Richard, H. Bender, M. Jurczak, and W. Vandervorst, Nano Lett. **14**, 2401 (2014).
[11]K. Atamanuk, J. Luria, and B. D. Huey, Beilstein J. Nanotechnol. **9**, 1802 (2018).
[12]A. Schulze, T. Hantschel, A. Dathe, P. Eyben, X. Ke, and W. Vandervorst, Nanotechnology **23**, 305707 (2012).
[13]J. Luria, Y. Kutes, A. Moore, L. Zhang, E. A. Stach, and B. D. Huey, Nat. Energy **1**, 16150 (2016).
[14]H. Han, Y. Kim, M. Alexe, D. Hesse, and W. Lee, Adv. Mater. **23**, 4599 (2011).
[15]D. Karpov, Z. Liu, T. d. S. Rolo, R. Harder, P. V. Balachandran, D. Xue, T. Lookman, and E. Fohtung, Nat. Commun. **8**, 280 (2017).
[16]T. Kämpfe, P. Reichenbach, A. Haußmann, T. Woike, E. Soergel, and L. M. Eng, Appl. Phys. Lett. **107**, 152905 (2015).
[17]C. Godau, T. Kämpfe, A. Thiessen, L. M. Eng, and A. Haußmann, ACS Nano **11**, 4816 (2017).
[18]J. J. Steffes, R. A. Ristau, R. Ramesh, and B. D. Huey, Proc. Natl. Acad. Sci. U.S.A. **116**, 2413 (2019).
[19]J. Y. Son, Y.-S. Shin, S.-W. Song, Y.-H. Shin, and H. M. Jang, J. Phys. Chem. C **115**, 14077 (2011).
[20]L. Ye, *Ferroelectric Switching and d_{33} Mapping of Micro-Patterned Piezoelectrics by Piezo Force Microscopy* (University of Connecticut, 2016).
[21]J. F. Scott, Science **315**, 954 (2007).
[22]G. Catalan, J. Seidel, R. Ramesh, and J. F. Scott, Rev. Mod. Phys. **84**, 119 (2012).
[23]I. Vrejoiu, M. Alexe, D. Hesse, and U. Gösele, J. Vac. Sci. Technol. B **27**, 498 (2009).
[24]D. G. Schlom, L.-Q. Chen, C. J. Fennie, V. Gopalan, D. A. Muller, X. Pan, R. Ramesh, and R. Uecker, MRS Bull. **39**, 118 (2014).
[25]D. Edwards, S. Brewer, Y. Cao, S. Jesse, L.-Q. Chen, S. V. Kalinin, A. Kumar, and N. Bassiri-Gharb, Adv. Mater. Interfaces **3**, 1500470 (2016).
[26]V. Nagarajan, A. Roytburd, A. Stanishevsky, S. Prasertchoung, T. Zhao, L. Chen, J. Melngailis, O. Auciello, and R. Ramesh, Nat. Mater. **2**, 43 (2003).
[27]A. B. Naden, D. Edwards, S. M. Neumayer, J. G. M. Guy, B. J. Rodriguez, N. Bassiri-Gharb, and A. Kumar, Adv. Mater. Interfaces **5**, 1801019 (2018).
[28]A. Morelli, F. Johann, S. R. Burns, A. Douglas, and J. M. Gregg, Nano Lett. **16**, 5228 (2016).
[29]J. A. Klug, M. V. Holt, R. N. Premnath, A. Joshi-Imre, S. Hong, R. S. Katiyar, M. J. Bedzyk, and O. Auciello, Appl. Phys. Lett. **99**, 052902 (2011).
[30]L. Zhao, Z. Lu, F. Zhang, G. Tian, X. Song, Z. Li, K. Huang, Z. Zhang, M. Qin, S. Wu, X. Lu, M. Zeng, X. Gao, J. Dai, and J.-M. Liu, Sci. Rep. **5**, 9680 (2015).
[31]Y. Kim, Y. Kim, H. Han, S. Jesse, S. Hyun, W. Lee, S. V. Kalinin, and J. K. Kim, J. Mater. Chem. C **1**, 5299 (2013).
[32]C. S. Ganpule, A. Stanishevsky, Q. Su, S. Aggarwal, J. Melngailis, E. Williams, and R. Ramesh, Appl. Phys. Lett. **75**, 409 (1999).
[33]M. Alexe, C. Harnagea, D. Hesse, and U. Gösele, Appl. Phys. Lett. **75**, 1793 (1999).
[34]S. Kim, Y. Bastani, H. Lu, W. P. King, S. Marder, K. H. Sandhage, A. Gruverman, E. Riedo, and N. Bassiri-Gharb, Adv. Mater. **23**, 3786 (2011).
[35]A. Kholkin, A. Morozovska, D. Kiselev, I. Bdikin, B. Rodriguez, P. Wu, A. Bokov, Z.-G. Ye, B. Dkhil, L.-Q. Chen, M. Kosec, and S. V. Kalinin, Adv. Funct. Mater. **21**, 1977 (2011).
[36]S. Hong, B. Ecabart, E. L. Colla, and N. Setter, Appl. Phys. Lett. **84**, 2382 (2004).
[37]V. Y. Shur, A. R. Akhmatkhanov, and E. V. Pelegova, Ferroelectrics **500**, 76 (2016).
[38]V. Y. Shur, E. I. Shishkin, E. V. Nikolaeva, M. S. Nebogatikov, D. O. Alikin, P. S. Zelenovskiy, M. F. Sarmanova, and M. A. Dolbilov, Ferroelectrics **398**, 91 (2010).
[39]S. R. Burns, J. M. Gregg, and V. Nagarajan, Adv. Funct. Mater. **26**, 8367 (2016).
[40]A. A. Tseng, J.-I. Shirakashi, S. Nishimura, K. Miyashita, and Z. Li, J. Nanosci. Nanotechnol. **10**, 456 (2010).
[41]M. Malekian, S. S. Park, D. Strathearn, M. G. Mostofa, and M. B. G. Jun, J. Micromech. Microeng. **20**, 115016 (2010).
[42]Y. Yan, Y. He, Y. Geng, Z. Hu, and H. Li, Curr. Nanosci. **12**, 666 (2016).
[43]Y. He, Y. Yan, Y. Geng, and E. Brousseau, Appl. Surf. Sci. **427**, 1076 (2018).
[44]J. X. Zhang, B. Xiang, Q. He, J. Seidel, R. J. Zeches, P. Yu, S. Y. Yang, C. H. Wang, Y.-H. Chu, L. W. Martin, A. M. Minor, and R. Ramesh, Nat. Nanotechnol. **6**, 98 (2011).
[45]D. Edwards, N. Browne, K. M. Holsgrove, A. B. Naden, S. O. Sayedghaee, B. Xu, S. Prosandeev, D. Wang, D. Mazumdar, M. Duchamp, A. Gupta, S. V. Kalinin, M. Arredondo, R. G. P. McQuaid, L. Bellaiche, J. M. Gregg, and A. Kumar, Nanoscale **10**, 17629 (2018).
[46]H. J. Lee, S. Zhang, J. Luo, F. Li, and T. R. Shrout, Adv. Funct. Mater. **20**, 3154 (2010).
[47]J. E. Sader, J. W. M. Chon, and P. Mulvaney, Rev. Sci. Instrum. **70**, 3967 (1999).
[48]G. A. Matei, E. J. Thoreson, J. R. Pratt, D. B. Newell, and N. A. Burnham, Rev. Sci. Instrum. **77**, 083703 (2006).
[49]V. Bykov, A. Gologanov, and V. Shevyakov, Appl. Phys. A **66**, 499 (1998).
[50]J. S. Villarrubia, J. Res. Natl. Inst. Stand. Technol. **102**, 425 (1997).
[51]B. J. Rodriguez, C. Callahan, S. V. Kalinin, and R. Proksch, Nanotechnology **18**, 475504 (2007).
[52]Y. Geng, Y. Yan, Y. Xing, X. Zhao, and Z. Hu, Int. J. Mach. Tool Manuf. **73**, 87 (2013).
[53]V. N. Koinkar and B. Bhushan, J. Mater. Res. **12**, 3219 (1997).
[54]A. Lugstein, B. Basnar, J. Smoliner, and E. Bertagnolli, Appl. Phys. Res. **76**, 545 (2003).
[55]A. A. Tseng, J. Micromech. Microeng. **14**, R15 (2004).
[56]Z. Q. Wang, N. D. Jiao, S. Tung, and Z. L. Dong, Appl. Surf. Sci. **257**, 3627 (2011).
[57]P. Sharma, Y. Heo, B.-K. Jang, Y. Liu, V. Nagarajan, J. Li, C.-H. Yang, and J. Seidel, Adv. Mater. Interfaces **3**, 1600033 (2016).
[58]P. Sharma, K. R. Kang, B.-K. Jang, C.-H. Yang, and J. Seidel, Adv. Electron. Mater. **2**, 1600283 (2016).
[59]Y. Heo, S. Hu, P. Sharma, K.-E. Kim, B.-K. Jang, C. Cazorla, C.-H. Yang, and J. Seidel, ACS Nano **11**, 2805 (2017).
[60]J. E. Sader, Rev. Sci. Instrum. **74**, 2438 (2003).
[61]J. L. Gilbert and J. D. Wernle, in *UHMWPE Biomaterials Handbook*, 3rd ed., edited by S. M. Kurtz (William Andrew Publishing, Oxford, 2016), pp. 772–785.
[62]S. Jesse, A. P. Baddorf, and S. V. Kalinin, Appl. Phys. Lett. **88**, 062908 (2006).
[63]A. Morelli, F. Johann, N. Schammelt, D. McGrouther, and I. Vrejoiu, J. Appl. Physiol. **113**, 154101 (2013).
[64]D. Liu, M. Chelf, and K. W. White, Acta Mater. **54**, 4525 (2006).
[65]G. A. Schneider, T. Scholz, and F. J. Espinoza-Beltrán, Appl. Phys. Lett. **92**, 022906 (2008).
[66]G. A. Schneider, T. Scholz, J. Muñoz-Saldaña, and M. V. Swain, Appl. Phys. Lett. **86**, 192903 (2005).
[67]B. Huang, Z. Li, and J. Li, Nanoscale **10**, 21320 (2018).
[68]M. Ziatdinov, O. Dyck, A. Maksov, X. Li, X. Sang, K. Xiao, R. R. Unocic, R. Vasudevan, S. Jesse, and S. V. Kalinin, ACS Nano **11**, 12742 (2017).
[69]X. Kong, P. H. Cohen, and J. Dong, J. Manuf. Processes **24**, 338 (2016).
[70]D. Teixidor, M. Grzenda, A. Bustillo, and J. Ciurana, J. Intell. Manuf. **26**, 801 (2015).
[71]P. Vettiger, G. Cross, M. Despont, U. Drechsler, U. Durig, B. Gotsmann, W. Haberle, M. A. Lantz, H. E. Rothuizen, R. Stutz, and G. K. Binnig, IEEE Trans. Nanotechnol. **1**, 39 (2002).
[72]Y. F. Gu, H. Harada, and Y. Ro, JOM **56**, 28 (2004).
[73]Y. Kim, H. Han, B. J. Rodriguez, I. Vrejoiu, W. Lee, S. Baik, D. Hesse, and M. Alexe, J. Appl. Physiol. **108**, 042005 (2010).
[74]A. V. Ievlev, S. KC, R. K. Vasudevan, Y. Kim, X. Lu, M. Alexe, V. R. Cooper, S. V. Kalinin, and O. S. Ovchinnikova, Nat. Commun. **10**, 3064 (2019).

Published under license by AIP Publishing.

Supplementary Information

Investigation of AFM-based machining of ferroelectric thin films at the nanoscale

Fengyuan Zhang,[1,2] David Edwards,[1,2] Xiong Deng,[3] Yadong Wang,[3] Jason I. Kilpatrick,[1,2] Nazanin Bassiri-Gharb,[4,5] Amit Kumar,[6] Deyang Chen,[3] Xingsen Gao,[3] and Brian J. Rodriguez[1,2]

[1] School of Physics, University College Dublin, Belfield, Dublin D04 V1W8, Ireland
[2] Conway Institute of Biomolecular and Biomedical Research, University College Dublin, Belfield, Dublin 4, Ireland
[3] Institute for Advanced Materials, South China Academy of Advanced Optoelectronics, Guangzhou, People's Republic of China
[4] School of Materials Science and Engineering, Georgia Institute of Technology, Atlanta, USA
[5] George W. Woodruff School of Mechanical Engineering, Georgia Institute of Technology, Atlanta, USA
[6] Centre for Nanostructured Media, School of Mathematics and Physics, Queen's University Belfast, UK

Removal of Residual Pile-up

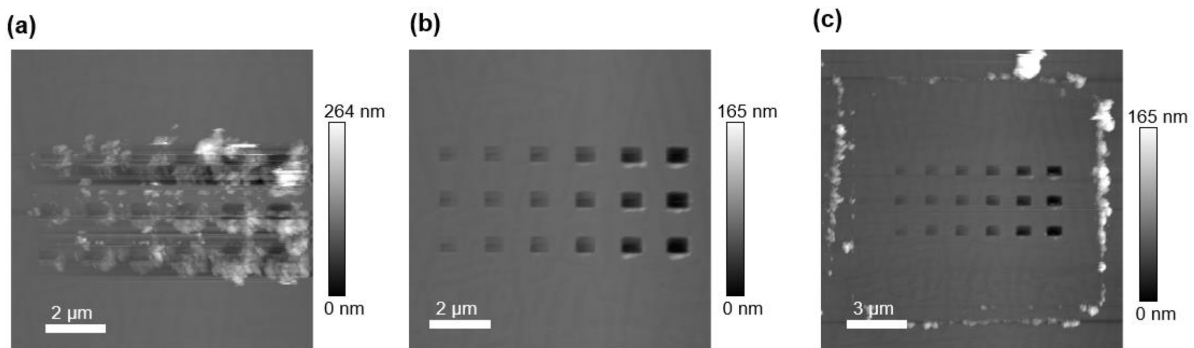

Fig. S1. Demonstration of pile-up removal after machining. (a) Amplitude modulation mode image after machining the array of squares shown in Figure 2b of the main text. (b) Contact mode image at a normal imaging force (< 0.5 µN) immediately afterwards during the cleaning pass. Such a loading force is well below the ~ 10 µN required for machining with the same tip. (c) Amplitude modulation mode image over a larger area after the cleaning image had finished, demonstrating how the machined residue was moved to the perimeter of the cleaning image. All images were obtained with the same diamond tip used for machining.

Determining the Tip Shape

To determine and monitor the shape of the diamond tips used for machining, amplitude modulation mode images of a tip characterization grating (TGT101, MikroMasch, Germany) were obtained before and after each machining experiment. The blind reconstruction technique[1] implemented in Gwyddion,[2] was then used to reconstruct the tip shape. 3D images of both the NM-RC and NM-TC tip apexes are shown in Figures S2(a) and S2(c), respectively, in their "initial" states before the machining experiments were carried out. The cross-sectional areas (A) of both of the reconstructed tips were then calculated as a function depth (distance from the tip apex) and converted into an effective radius R, where

$$R = \sqrt{\frac{A}{\frac{2}{\pi}}}$$

The effective radius of both tips in their "initial" and "final" states after all machining experiments are shown in Figures S2(e) and S2(f). It should be noted that some preliminary machining experiments were carried out using these tips prior to the definition of the "initial" state, so as to wear down the apex of the tip slightly down to a more "stable" regime and ensure increased repeatability of the machining behavior. As evident, a relatively small amount of tip degradation occurred over the entire course of the machining experiments shown in this work, with the effective radius of the NM-RC tip increasing by ~10% and the NM-TC tip increasing by ~3%. The radius of the most accurate approximation for each tip is also shown by the dashed lines in Figures S2(e) and S2(f). The NM-RC tip was used for the bulk of the machining experiments in the main text (from Figure 2 onwards in the main text).

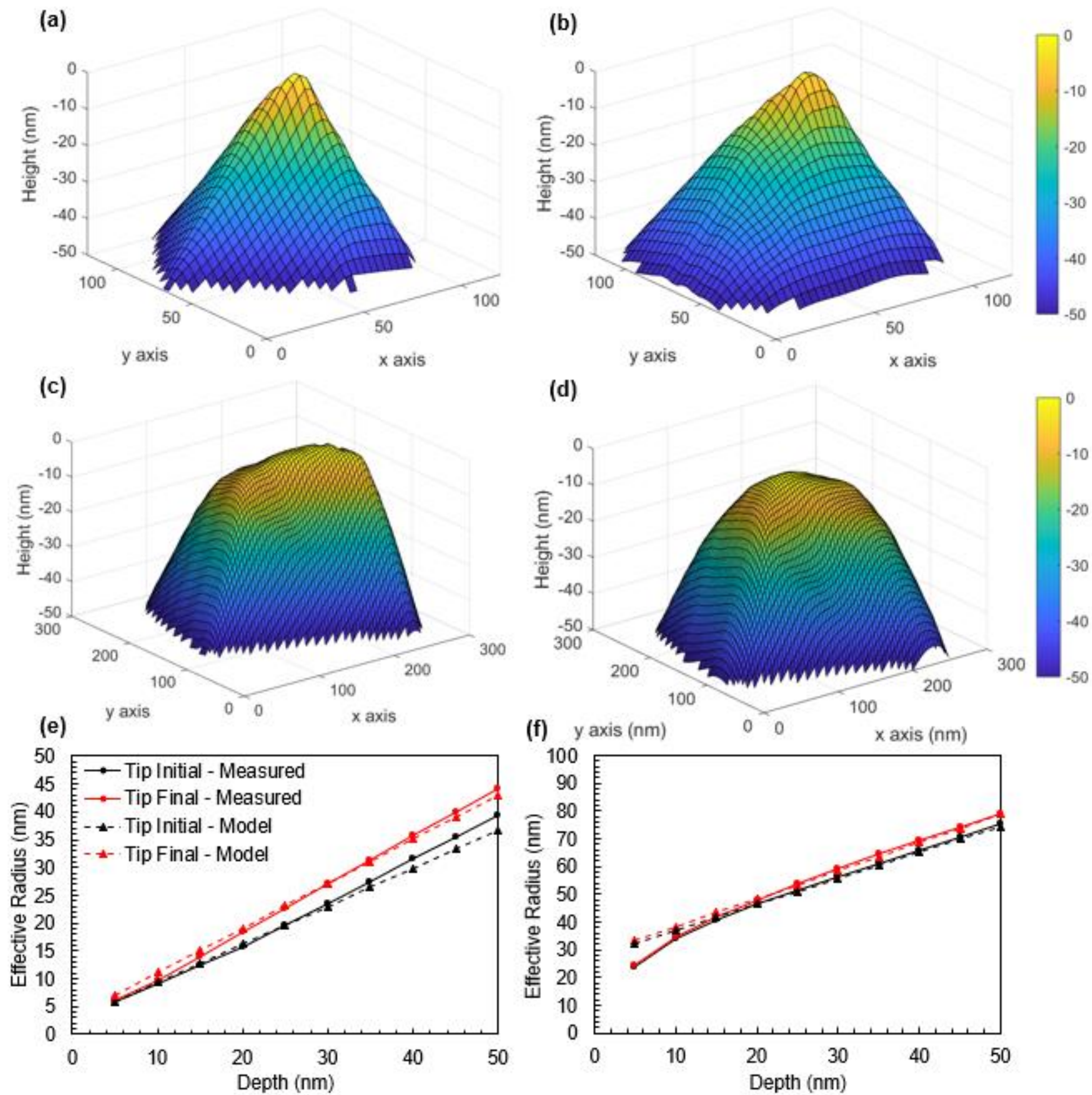

Fig. S2. Tip reconstructions at various stages. (a) 3D image of the NM-RC tip before and (b) after it was used for the machining experiments shown in the main text. (c) Reconstructed 3D image of the NM-TC tip apex before and (d) after it was used for the machining experiments shown in the main text. It can be noted that the x axis is parallel to the cantilever long axis, while the y axis is parallel to the cantilever short axis. The effective radius of the reconstructed (e) NM-RC tip (f) and NM-TC tip as a function of depth from the apex. The radius of the tip is plotted both before (black) and after (red) all machining operations were carried out. A model of the tip shape is also shown by the dashed lines. For the NM-RC tip, the tip was best modelled by a rounded, conical tip with a 2.5 nm radius and 43° tip half angle initially, and a 3 nm radius and a 52° tip half angle after machining. For the NM-TC tip, the tip was best modelled by a truncated cone with 39 nm radius and 53° tip half angle initially, and a 40 nm radius and a 55° tip half angle after machining.

Extracting Mechanical Properties

To provide insight into and predict machining behavior in the $BiFeO_3$ film, extraction of the mechanical properties of the film is of particular use. For instance, the yield stress for plastic indentation can help predict loading forces required to begin machining the film. These mechanical properties can be obtained at the nanoscale using the same AFM tips for nanoindentation. Figure 3(a) shows an initial topography image of a region of the film showing a mixture of dark needle-like structures comprising the rhombohedral-like R phase, interspersed within a raised matrix comprising the tetragonal-like T phase typical of mixed phase $BiFeO_3$.[3] An array of nanoindentations was then carried out, with the maximum applied load varied along the vertical axis, and probe velocity varied along the horizontal axis. For each nanoindentation, the maximum loading force was set as a trigger event upon which a change in tip direction would occur. In the resulting topography image in Figure 3(b), a number of additional R phase needles were observed nucleated around the regions where nanoindentations were carried out. Such an observation is consistent with observations of T to R phase transformations under sufficient loads (several hundred nN) in literature.[4,5] Meanwhile, plastic indentation appears to occur at 30 μN and above. The indentations show an oval-like shape, due to tip translation under loading. Such an effect can result in artefacts in nanoindentation data which may be corrected by applying a compensating x-piezo motion[6] (not done as part of this work).

Two example nanoindentation measurements, highlighted in Figure 3(b) by the red and green circles, are shown in Figures 3(c) and 3(d), respectively. As evident in the extension curves, a number of rapid changes in behavior occur at larger forces. Even for the force curves where no plastic indentation in observed, a substantial increase in the gradient begins above ~ 8 μN. This is likely an effect of the mechanically-induced transition from T- to R-phase transition as evident by the increased R phase population after the force curves were obtained. It should be noted, however, that as this transition is reversible under an electric field,[7] it does not signify the onset of plastic deformation. At larger forces meanwhile, additional changes occur in the form of pop-in events due to plastic deformation above 20 μN (as indicated in Figure 3(d)). Due to the ascribed behavior and resulting possible artefacts in the nanoindentation curves, the curves were considered to be not suitable for fitting with models in order to extract a Young's modulus value. Previous studies on mixed phase $BiFeO_3$ have reported values varying from 10 – 70 GPa.[5,8]

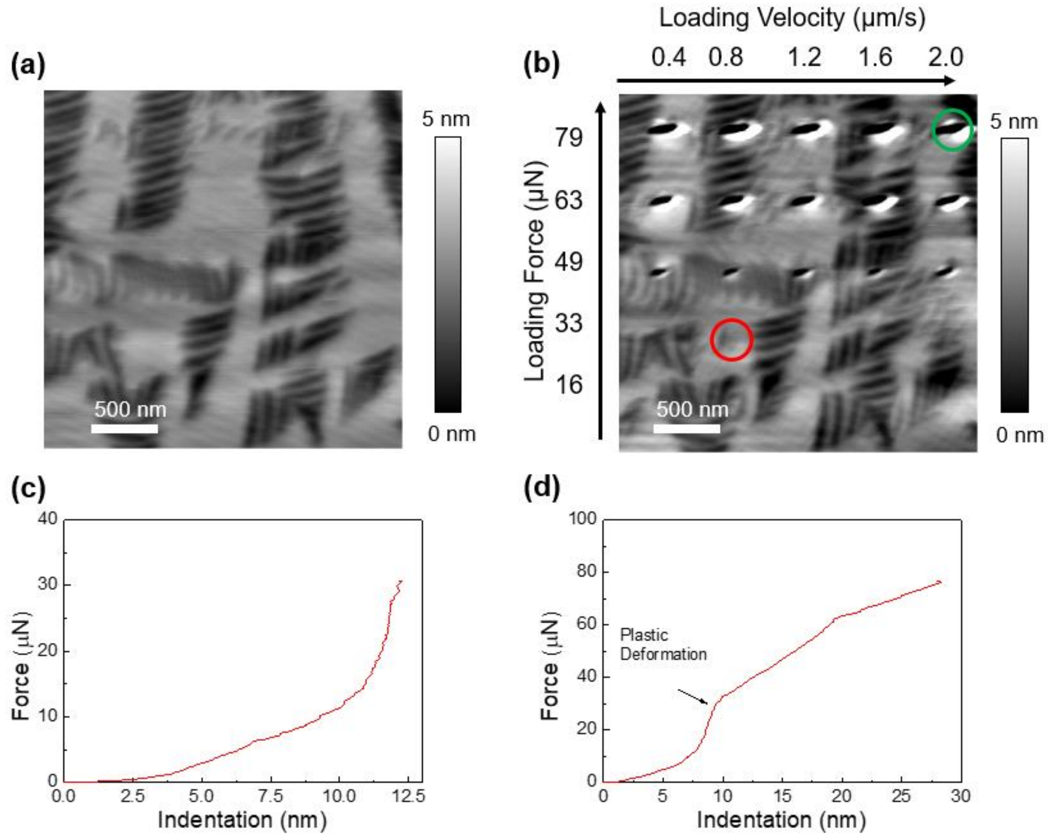

Fig. S3. Nanoindentation of mixed phase $BiFeO_3$. Topography (a) before and (b) after nanoindentation at varying maximum load and velocity. Nanoindentation profiles from the points highlighted by the (c) red and (d) green circle.

The yield force for plastic indentation was identified from the curves and the contact area estimated from a reconstructed profile of the tip. The force at which plastic indentation occurs is evident by the sudden decrease in the force indentation gradient above ~ 30 μN. From each of the force indentation curves acquired, the average yield force (F_y) was found to be 33.2 ± 3.3 μN and occurs at an average indentation of 8.6 ± 0.9 nm. The relatively small uncertainties (~ 10%) despite the spatial variation in initial mixed phase population and resulting levels of tip translation, indicates that these factors have a sufficiently minimal effect on F_y. From the reconstructed tip profile before the indentation measurement was carried out, the tip area A is 481 ± 65 nm^2 at 8.6 ± 0.9 nm from the tip apex with the uncertainty propagating from the variation in the depth at which F_y occurs. Approximating the yield stress (σ_y) from the relation, $\sigma_y = F_y/A$ results in an estimated yield stress of 71.1 ± 15.9 GPa. Comparing the extracted value of σ_y to those obtained on other ferroelectric materials, the σ_y measured here is significantly larger than those obtained via microindentation experiments.[9] The likely overestimation observed here may be due to the indentation geometries, with the sharper probe and contact radius used here giving rise to a different concentration of stress fields compared to microindentation experiments.[10] However, as a similar tip geometry is used for subsequent machining experiments carried out in this work, the extracted value should provide an appropriate approximation for predicting the subsequent machining behavior, as observed in the agreement with experimental data at higher loads.

Determining Film Thickness

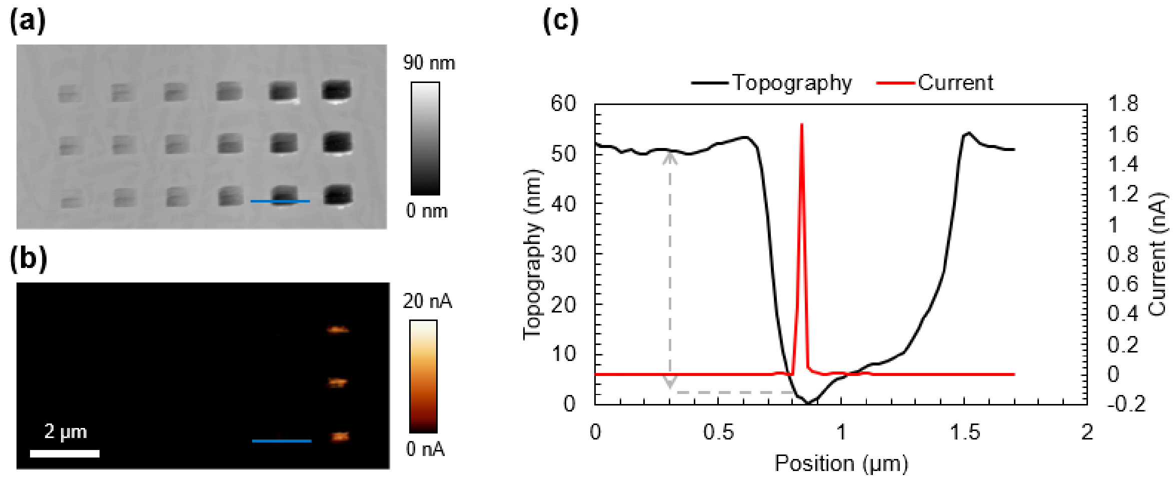

Fig. S4. Determining film thickness. (a) Topography and (b) corresponding cAFM image of the machined squares shown in Figure 1b of the main text. The cAFM was obtained using a 1 V bias to the bottom electrode, with a 500 MΩ resistor in series. The line profiles from the blue lines are shown in (c). Evident that the current increases sharply at a depth close to 50 nm, as indicated by the grey dashed lines. From a study of a range of different line profiles across various regions of the image the film thickness was estimated as 48 ± 1 nm. The dark line within thinned regions is attributed to an extra line pass in lithography mode.

Lateral Cantilever Spring Constants

From a study by J. E. Sader,[11] the spring constants parallel to the cantilever long (k_x) and short (k_y) axis, respectively, are given as:

$$k_x = \frac{1}{h^2}\frac{k_\theta k_{z\theta}^2}{k_{z\theta}^2 - k_z k_\theta}, \qquad k_x = \frac{k_\varphi}{h^2}$$

where h is the distance from the midplane of the cantilever (13 µm used here) and the tip apex. k_z describes the normal spring constant, $k_{z\theta}$ and k_θ describe two of the longitudinal spring constants, while k_φ describes the torsional spring constant. The spring constants are dependent on cantilever length (136.5 µm used here), thickness (4 µm), and width (38.8 µm), as well as the Young's modulus (800 GPa) and Poisson's ratio (0.2) of the cantilever.[11]

Effect of Varying Machining Angle

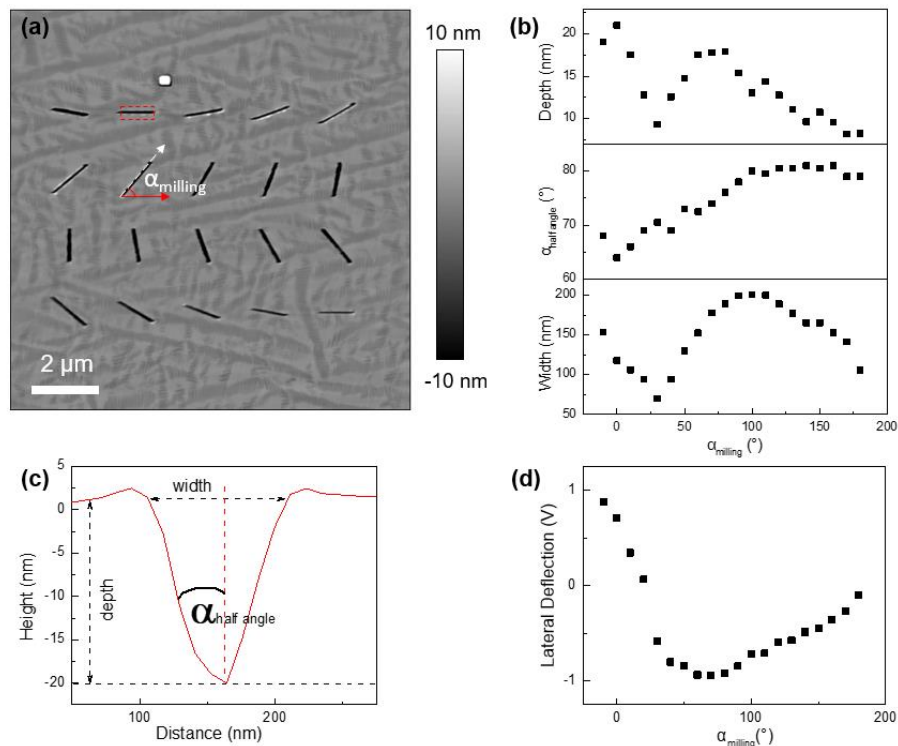

Fig. S5. (a) Topography after machining single lines at varying scan angles. The red arrow runs parallel to the cantilever long axis while the white arrow indicates the direction of tip motion. α_m was defined as the angle between these two arrows. (b) Plots of depth, α_{ha} and width as a function of machining angle. Again, the sharpest (deepest with lowest half angle) line is machined around where $\alpha_m = 0$º. The depth, α_{ha} and width are determined by the average line profile across the machined scratch. The inset image in (b) shows an example of the line profile across the dashed red box in (a).

Role of Tip Velocity on Machining Behavior

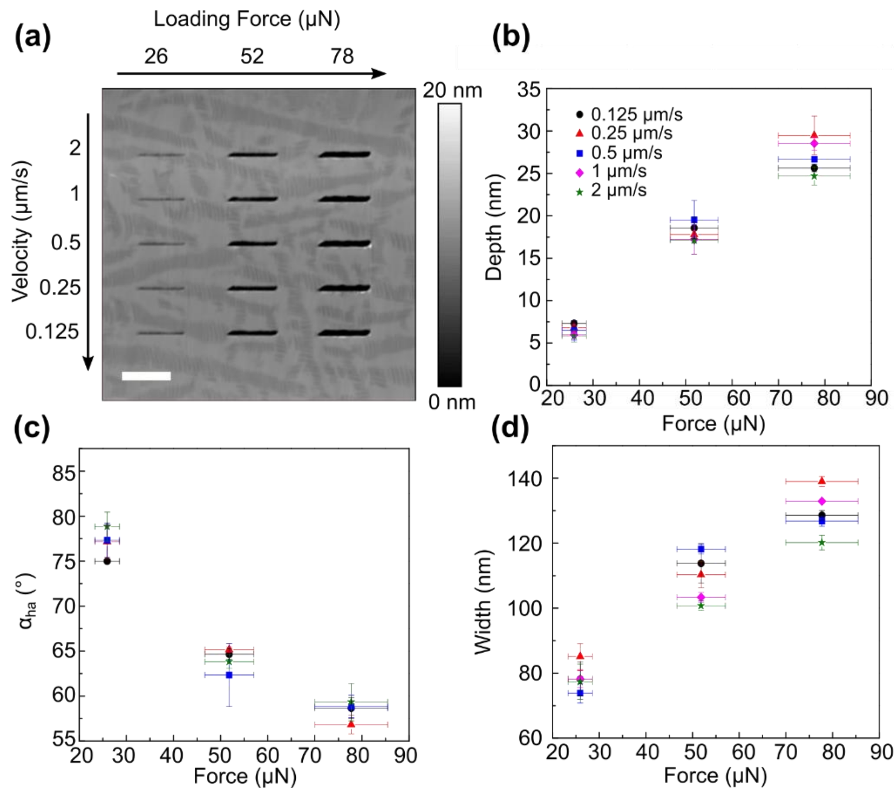

Fig. S6. The effect of tip velocity and loading force at a constant machining angle (lines machined in order from fastest to slowest velocities (in reverse order of Figure 3)). (a) The topography of a 5 × 5 μm region of the film after machining a series of lines that are 1 μm in length. (b) Machined depth, (c) half angle and (d) width as analyzed from (a) as a function of loading force for different tip velocities. As evident, when carrying out the experiment in reverse order to Figure 3 in the main text, the slowest tip velocity no longer gives rise to the deepest and narrowest depths. The scale bar is 1 μm.

Studying the Machined Nanoislands

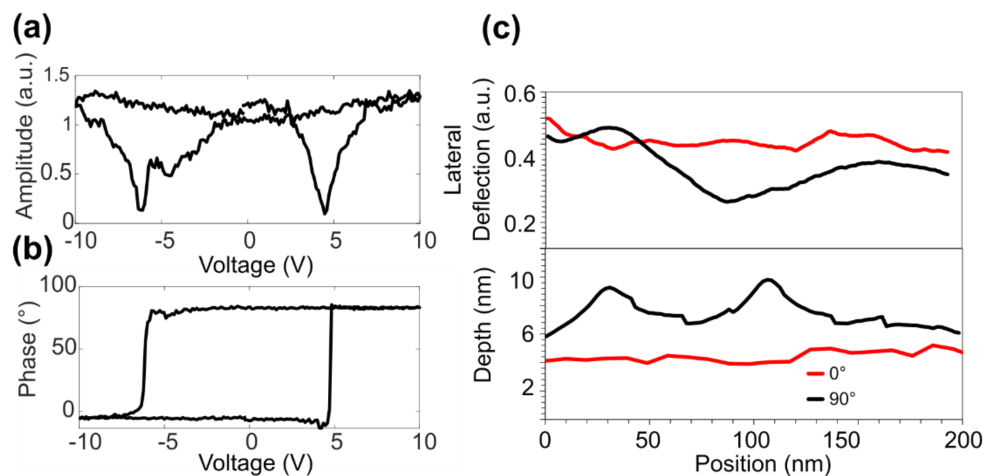

Fig. S7. Measured VPFM (a) amplitude and (b) phase hysteresis loops on the as-grown regions of the film. (c) Lateral deflection of the cantilever during machining of the first pair machined lines ($\alpha_m = 0°$) and second pair of machined lines ($\alpha_m = 90°$) with 90 nm separation. At $\alpha_m = 0°$, the lateral deflection is relatively constant, while at $\alpha_m = 90°$ it takes a sudden dip after crossing over the previously machined lines.

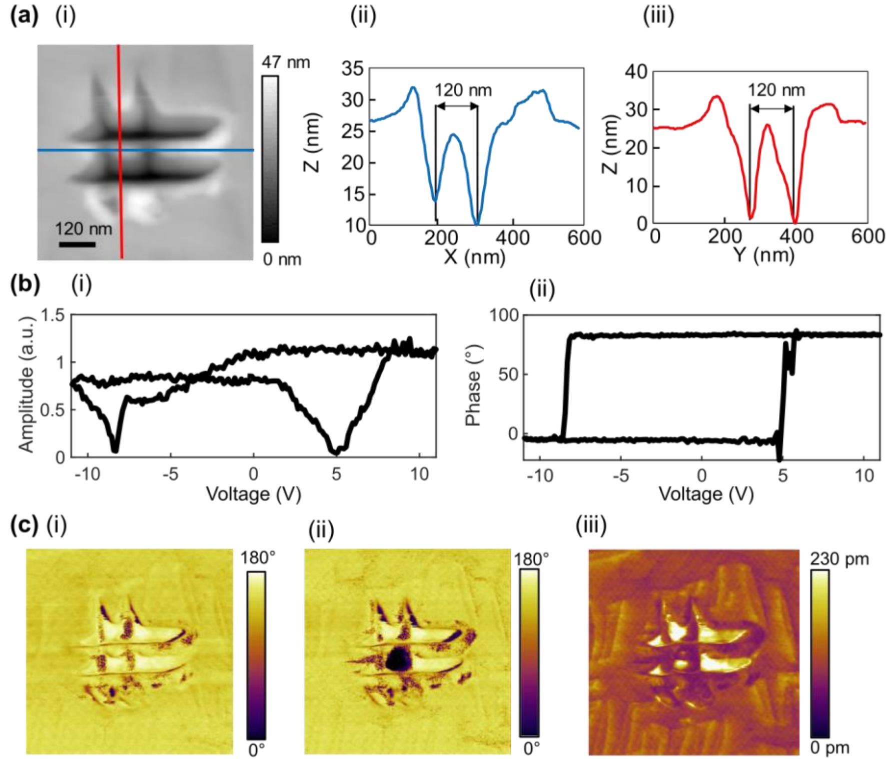

Fig. S8. (a) (i) Topography after fabricating a 120 nm nanoisland with line profiles corresponding to the (ii) red and (iii) blue lines. (b) (i) VPFM amplitude and (ii) phase loop on the island. (c) VPFM phase image (i) before and (ii) after acquisition of the hysteresis loop, showing reversal of the measured phase from pointing down to up. (iii) VPFM amplitude after loop acquisition showing a minimum in amplitude around the switched domain corresponding to the induced domain wall.

Investigation of AFM-based Machining on a Top Electrode

An array of lines was machined on a Cr-Au coated $BiFeO_3$ film with $\alpha_m = 0°$ at varying loading forces and scan speeds as shown in the resulting AFM topography image in Figure S9(a). The $BiFeO_3$-Cr-Au film shown here has an electrode with 5 nm of Cr followed by 0.5 nm Au and is different to the one shown in the main text. The measured line depths and widths are then plotted in Figures S9(b) and S9(c), respectively. In contrast to the more linear increase in depth at lower forces (< 25 μN) on the bare surface, a more gradual increase in depth is observed on the electrode up until a threshold of 22.5 μN, where a depth close to 5 nm is reached. Beyond this threshold, the depth increases more rapidly. This behavior could be due to the difference in mechanical properties between Cr and $BiFeO_3$, where Cr has a yield stress of 430 MPa, which is much softer than the 71.1 GPa estimated here for $BiFeO_3$. Meanwhile, the behavior of the width with varying loading forces is similar to that observed on the bare film. A nanocapacitor array was also fabricated on the $BiFeO_3$-Cr-Au film described above and is shown in Figure S9(d), where a series of lines were machined by scanning an array with 20 μN at 1 μm/s with a 150 nm line separation. This electrode showed better adhesion to the $BiFeO_3$ surface compared to that shown in the main text, possibly due to the surface being cleaner before metal deposition. However, the underlying $BiFeO_3$ film suffered problems relating to dielectric breakdown near the coercive field and was grown with a $LaSrMnO_3$ bottom electrode as opposed to the film in the main text which possesses a $Ca_{0.67}Ce_{0.33}MnO_3$ bottom electrode.

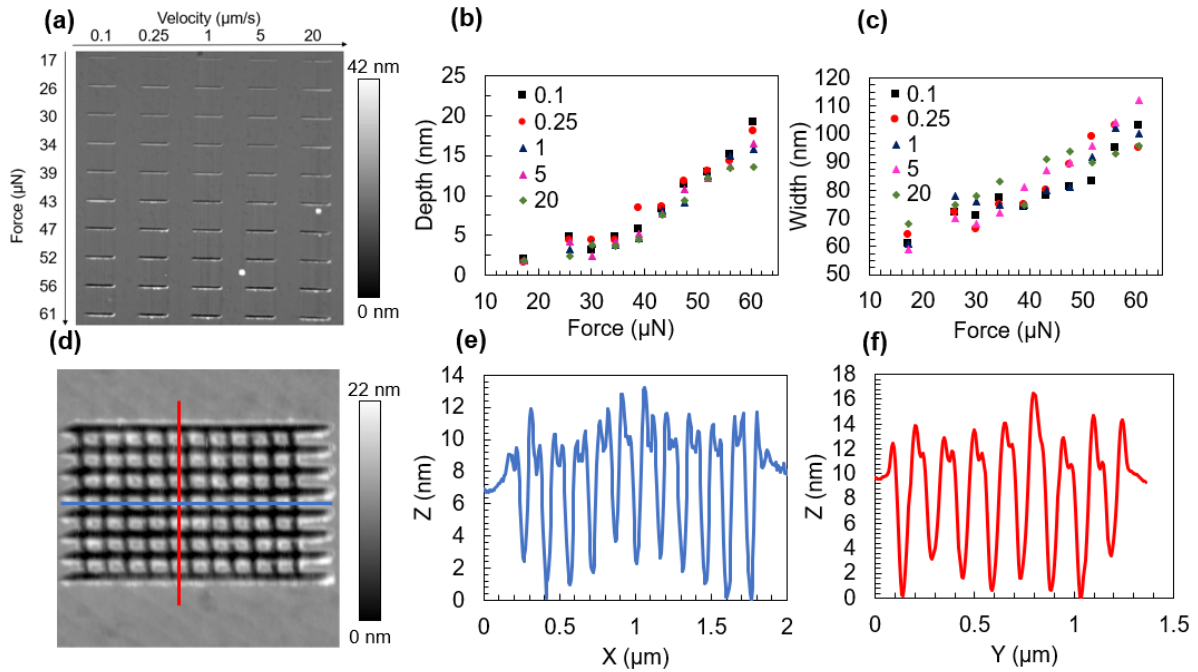

Fig. S9. Fabrication of a nanocapacitor array. (a) Topography after scanning an array of single lines with varying loading forces and tip velocities. The measured (b) depth and (c) width of the machined lines. Topography of a nanocapacitor array with the corresponding line profile along the (e) y axis (in blue) and (f) x axis in red showing that the tip has machined through the thickness of the top electrode, creating individual capacitor elements.

References

[1] J.S. Villarrubia, J. Res. Natl. Inst. Stand. Technol. **102**, 425 (1997).

[2] D. Nečas and P. Klapetek, Cent. Eur. J. Phys. **10**, 181 (2012).

[3] R.J. Zeches, M.D. Rossell, J.X. Zhang, A.J. Hatt, Q. He, C.-H. Yang, A. Kumar, C.H. Wang, A. Melville, C. Adamo, G. Sheng, Y.-H. Chu, J.F. Ihlefeld, R. Erni, C. Ederer, V. Gopalan, L.Q. Chen, D.G. Schlom, N.A. Spaldin, L.W. Martin, and R. Ramesh, Science **326**, 977 (2009).

[4] Y. Heo, B.-K. Jang, S.J. Kim, C.-H. Yang, and J. Seidel, Adv. Mater. **26**, 7568 (2014).

[5] P. Sharma, Y. Heo, B.-K. Jang, Y. Liu, V. Nagarajan, J. Li, C.-H. Yang, and J. Seidel, Adv. Mater. Interfaces **3**, 1600033 (2016).

[6] L. Huang, C. Meyer, and C. Prater, J. Phys.: Conf. Ser. **61**, 805 (2007).

[7] D. Edwards, N. Browne, K.M. Holsgrove, A.B. Naden, S.O. Sayedghaee, B. Xu, S. Prosandeev, D. Wang, D. Mazumdar, M. Duchamp, A. Gupta, S.V. Kalinin, M. Arredondo, R.G.P. McQuaid, L. Bellaiche, J.M. Gregg, and A. Kumar, Nanoscale **10**, 17629 (2018).

[8] Y. Heo, S. Hu, P. Sharma, K.-E. Kim, B.-K. Jang, C. Cazorla, C.-H. Yang, and J. Seidel, ACS Nano **11**, 2805 (2017).

[9] M. Algueró, A.J. Bushby, and M.J. Reece, J. Mater. Res. **16**, 993 (2001).

[10] A.C. Fischer-Cripps, *Introduction to Contact Mechanics* (Springer US, Boston, MA, 2007), pp. 77–100.

[11] J.E. Sader, Rev. Sci. Inst. **74**, 2438 (2003).